Journal of Computational Physics 229 (2010) 1994–2008

Contents lists available at ScienceDirect

Journal of Computational Physics

journal homepage: www.elsevier.com/locate/jcp

An adjoint method for shape optimization in unsteady viscous flows

D.N. Srinath, Sanjay Mittal *

Department of Aerospace Engineering, Indian Institute of Technology Kanpur, UP 208 016, India

ARTICLE INFO

Article history:
Received 15 June 2009
Received in revised form 15 October 2009
Accepted 10 November 2009
Available online 16 December 2009

Keywords:
Shape optimization
Adjoint methods
Unsteady flows
Time accurate
Finite element
Airfoil

ABSTRACT

A new method for shape optimization for unsteady viscous flows is presented. It is based on the continuous adjoint approach using a time accurate method and is capable of handling both inverse and direct objective functions. The objective function is minimized or maximized subject to the satisfaction of flow equations. The shape of the body is parametrized via a Non-Uniform Rational B-Splines (NURBS) curve and is updated by using the gradients obtained from solving the flow and adjoint equations. A finite element method based on streamline-upwind Petrov/Galerkin (SUPG) and pressure stabilized Petrov/Galerkin (PSPG) stabilization techniques is used to solve both the flow and adjoint equations. The method has been implemented and tested for the design of airfoils, based on enhancing its time-averaged aerodynamic coefficients. Interesting shapes are obtained, especially when the objective is to produce high performance airfoils. The effect of the extent of the window of time integration of flow and adjoint equations on the design process is studied. It is found that when the window of time integration is insufficient, the gradients are most likely to be erroneous.

1. Introduction

Increased computing capabilities and better algorithms in the last two decades have led to an increased interest in aerodynamic shape optimization. Many methods have been proposed and successfully utilized in the past. Some of them are random search methods [1], complex Taylor series expansion approach [2], automatic differentiation method [3], direct differentiation method [4] and adjoint based methods [5,6]. In adjoint based methods the cost of computing the gradients or sensitivities is independent of the number of design variables. These methods have found wide acceptance in aerodynamic shape optimization [7,8]. They have been utilized in various design applications in diverse areas such as aerospace [9–12], marine [13] and bio-medical engineering [14]. These methods attempt to seek the local optima in the design space. The possibility of the optimum being the global optima depends on the choice of the initial guess used in the optimization process. Srinath and Mittal [15] applied the adjoint based methods to optimize airfoils for aerodynamic performance in steady flow for $Re \leqslant 500$. Various objective functions, such as maximization of lift, minimization of drag and maximization of lift-to-drag ratio were considered. Very interesting shapes, especially at very low Re, were obtained. It was shown that the choice of objective function is vital to the results from the optimization process. The effect of imposing a volume constraint was also studied. Most of the effort in adjoint based methods has focused on design in the steady regime. Efforts in the optimization in unsteady flows have been few and fall in one of the two kinds: time accurate and frequency domain methods.

In time accurate methods the governing equations are solved in the time domain. We list some efforts in the past that have utilized this approach. He et al. [16] minimized the drag of a rotating cylinder at $Re = 200$ and 1000 by controlling

* Corresponding author. Tel.: +91 512 2597906; fax: +91 512 2597626.
E-mail addresses: srinath@iitk.ac.in (D.N. Srinath), smittal@iitk.ac.in (S. Mittal).

0021-9991/$ - see front matter © 2009 Elsevier Inc. All rights reserved.
doi:10.1016/j.jcp.2009.11.019

the frequency and amplitude of the angular velocity imparted to the cylinder. They used a direct objective function on the drag. Homescu et al. [17] applied the time accurate adjoint method to suppress Karman vortex shedding in the wake of a spinning cylinder at Re ranging from 60 to 1000. To obtain the optimal angular velocity that suppresses shedding, they used an objective function which minimizes the L_2 norm of the difference between the computed velocity and a desired velocity. The steady velocity field obtained at $Re = 2$ was used as the desired velocity. Okumura and Kawahara [18] applied the adjoint method to reduce the force on a $Re = 200$ flow past a circular cylinder. A streamlined shape was achieved as a consequence of drag reduction. Nadarajah and Jameson [19] compared the result of a full unsteady optimization with that of a multi-point approach for the design of a pitching airfoil in an unsteady inviscid flow. In the multi-point approach the unsteady flow and the corresponding adjoint variables are replaced with the steady quantities at each time step. They observed that both the methods yield similar results for low pitch frequency of the airfoil. However, significantly different values of the gradient are obtained from the two methods for higher frequency of pitch oscillations. Mani and Mavriplis [20] also applied the adjoint method for shape optimization of a pitching airfoil in an inviscid flow. They used an Arbitrary Lagrangian–Eularian (ALE) formulation with deforming mesh. It was noticed that when the number of design variables is large, the optimizer is not able to achieve the prescribed convergence criteria. Convergence is achieved when the number of design variables is reduced. They attributed the problem to the complexity of the design space and the inability of the optimizer to navigate through it. Rumpfkeil and Zingg [21,22] carried out an inverse design of a multi-element airfoil at high angle of attack and $Re = 800$. The objective was to control the pressure in the near-field plane. They used flow fields only at intermittent time steps to compute the adjoint and gradient. They observed that if the information from a certain large number of time steps is skipped, then the optimizer is not able to converge. Collis et al. [23] extended optimization in unsteady flows to compressible flows. They analyzed the interaction of two counter-rotating vortices with a wall at $Re = 25$. The temporal and spatial distribution of velocity normal to the wall was used as the control. They noticed that the gradients are strongly dependent on the choice of the control space.

In the frequency domain methods [24,25] the governing equations are solved in the frequency domain. A Fourier transformation is used for the conversion from the time to frequency domain. Duta et al. [26] applied this method to reduce the blade vibration due to incoming unsteady flows for turbo-machinery applications. Nadarajah et al. [27] compared the time accurate method with the frequency domain method for the reduction of drag of an oscillating airfoil in an inviscid medium. They found that both the methods produce identical results. However, the frequency domain method is less expensive. It should be noted that the frequency domain methods are applicable only if the flow is periodic in time. Nadarajah and Tatossian [28] extended the frequency domain method to viscous flows. They minimized the drag of a helicopter rotor blade while maintaining a constant lift.

In the present work, a new method based on the continuous adjoint approach is formulated, implemented and demonstrated for the design of airfoils in an unsteady viscous flow. A stabilized finite element method based on streamline-upwind Petrov/Galerkin (SUPG) and pressure stabilized Petrov/Galerkin (PSPG)[29] stabilization techniques is employed to solve, both, the flow and the adjoint equations. The geometry of the airfoil is parametrized by a fourth order Non-Uniform Rational B-Splines (NURBS) curve [37]. The mesh close to the surface of the airfoil is structured while it is unstructured away from the airfoil. A reference mesh is generated and later deformed to accommodate new shapes via a mesh moving scheme [43]. In this scheme the modified equations of linear elasticity are solved to obtain internal nodal displacements based on the change in the shape of the surface. The Limited memory-Broyden–Fletcher–Goldfarb–Shanno (L-BFGS) algorithm [42] is used to minimize the objective function. The formulation is tested on two cases. The first involves an inverse objective function: to determine the shape of an airfoil that has a certain time-averaged lift coefficient at $Re = 1000$. The effect of varying the time-averaged lift coefficient on the shape of the airfoil is investigated. The second test case involves a direct objective function: to find the shape of an airfoil that has the least drag to lift ratio.

One of the challenges in unsteady flow optimization is to compute reasonably accurate gradients within the constraints of available computational resources. The issue of accuracy of the gradients has been analyzed by Nadarajah et al. [27] for inviscid flows. They computed the gradient by using the flow and adjoint solutions obtained over the last time period. The effect of the number of time steps in one time period on the accuracy of the gradient was studied. It was found that the accuracy of the gradient increases with increase in number of time steps in each time period.

The time period of unsteadiness is usually not known a priori. Therefore gradients must be estimated from flow computed for sufficiently long time. The effect of the extent of window, for time integration of flow and adjoint equations, on the optimization process is investigated in this study. The accuracy of gradients is also studied.

2. Governing equations

Let $\Omega \subset R^{n_{sd}}$ and $(0,T)$ be the spatial and temporal domains, respectively, where n_{sd} is the number of space dimensions.Let Γ represent the boundary of Ω. The spatial and temporal co-ordinates are denoted by $\boldsymbol{x}$ and t. The Navier–Stokes equations governing incompressible flow are

$$\rho\left(\frac{\partial \boldsymbol{u}}{\partial t} + \boldsymbol{u}\cdot\nabla\boldsymbol{u}\right) - \nabla\cdot\boldsymbol{\sigma} = 0 \quad \text{on } \Omega\times(0,T), \tag{1}$$

$$\nabla\cdot\boldsymbol{u} = 0 \quad \text{on } \Omega\times(0,T). \tag{2}$$

Here $\rho, \boldsymbol{u}$ and $\boldsymbol{\sigma}$ are the density, velocity and stress tensor, respectively. For a Newtonian fluid the stress tensor is given as $\boldsymbol{\sigma} = -p\boldsymbol{I} + \mu[\nabla\boldsymbol{u} + (\nabla\boldsymbol{u})^T]$ where, p is the pressure and $\boldsymbol{I}$ the identity tensor. The boundary conditions are either on the flow velocity or stress. Both, Dirichlet and Neumann type boundary conditions are considered in the following form:

$$\boldsymbol{u} = \boldsymbol{g} \quad \text{on } \Gamma_g, \tag{3}$$

$$\boldsymbol{n}\cdot\boldsymbol{\sigma} = \boldsymbol{h} \quad \text{on } \Gamma_h, \tag{4}$$

where, $\boldsymbol{n}$ is the unit normal vector on the boundary Γ. Here, Γ_g and Γ_h are the subsets of the boundary Γ. More details on the boundary conditions are given in Fig. 1. Γ_U, Γ_D and Γ_S represent the upstream, downstream and lateral boundaries, respectively. The surface of the body is represented by Γ_B.

The initial condition on the velocity is specified as:

$$\boldsymbol{u}(\boldsymbol{x}, 0) = \boldsymbol{u}_0 \quad \text{on } \Omega, \tag{5}$$

where $\boldsymbol{u}_0$ is divergence free.

The drag and lift force coefficients, (C_d, C_l), on the body are calculated using the following expression:

$$(C_d, C_l) = \frac{2}{\rho U^2 S}\int_{\Gamma_B} \boldsymbol{\sigma}\boldsymbol{n}\, d\Gamma. \tag{6}$$

The time-averaged coefficients are calculated as follows:

$$\overline{C_d} = \frac{1}{T}\int_{t_0}^{t_0+T} C_d(t)dt, \tag{7}$$

$$\overline{C_l} = \frac{1}{T}\int_{t_0}^{t_0+T} C_l(t)dt. \tag{8}$$

The time-averaging begins at $t = t_0$ to leave out the transient effect of the initial condition on the fully developed flow.

3. The adjoint approach

3.1. The augmented objective function

Let Γ_B be the segment of the boundary whose shape is to be determined. Let $\boldsymbol{\beta} = (\beta_1, \ldots, \beta_m)$ be the set of shape parameters that determine Γ_B. The optimization problem involves finding the shape parameters that minimize (or maximize) the objective function, $I_c(\boldsymbol{U}, \boldsymbol{\beta})$.

The flow Eqs. (1) and (2) are treated as constraint conditions on the objective function. An augmented objective function is constructed to convert the constrained problem to an unconstrained one. The flow equations are augmented to the objective function by introducing a set of Lagrange multipliers or adjoint variables $\boldsymbol{\Psi} = (\boldsymbol{\psi}_{\boldsymbol{u}}, \psi_p)$

$$I = I_c - \int_0^T\int_\Omega \psi_p \nabla\cdot\boldsymbol{u}\, d\Omega\, dt + \int_0^T\int_\Omega \boldsymbol{\psi}_{\boldsymbol{u}}\cdot\left(\rho\left(\frac{\partial\boldsymbol{u}}{\partial t} + \boldsymbol{u}\cdot\nabla\boldsymbol{u}\right) - \nabla\cdot\boldsymbol{\sigma}\right)d\Omega\, dt. \tag{9}$$

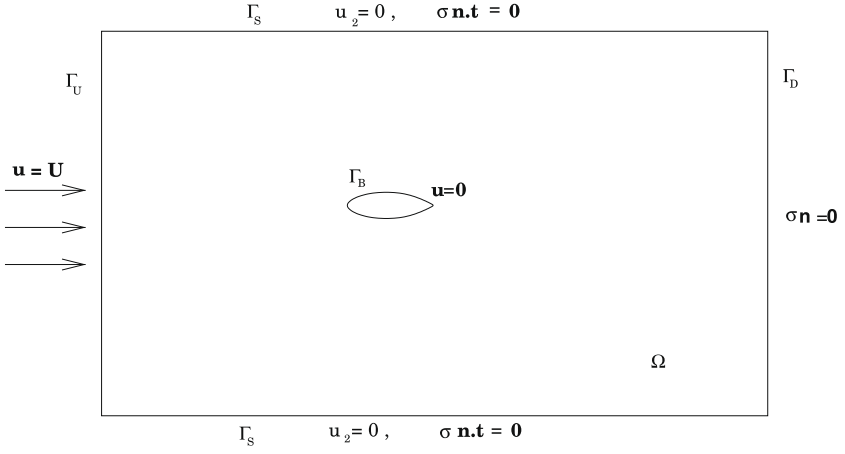

Fig. 1. Schematic of the problem set-up: boundary conditions. Γ_U, Γ_D and Γ_S are the upstream, downstream and lateral boundaries, respectively and Γ_B is the body surface.

The augmented objective function, is given by Eq. (9), degenerates to the original one if the flow variables, $\boldsymbol{U} = (\boldsymbol{u}, p)$, exactly satisfy Eqs. (1) and (2). The variables $\boldsymbol{\psi_u}$ and ψ_p are referred to as the adjoint velocity and adjoint pressure, respectively. The first variation of the augmented objective function is given by:

$$\delta I = \frac{\partial I}{\partial \boldsymbol{U}}\delta \boldsymbol{U} + \frac{\partial I}{\partial \boldsymbol{\beta}}\delta \boldsymbol{\beta} + \frac{\partial I}{\partial \boldsymbol{\Psi}}\delta \boldsymbol{\Psi}. \tag{10}$$

The optimal solution is achieved when the variation of the augmented objective function vanishes, i.e., $\delta I = 0$. This requires that the variation of I with respect to the flow variables $\boldsymbol{U}$, design parameters $\boldsymbol{\beta}$ and the adjoint variables $\boldsymbol{\Psi}$ should go to zero, independently. Variation of I with respect to $\boldsymbol{U}$ is given by:

$$\frac{\partial I}{\partial \boldsymbol{U}} = \frac{\partial I_c}{\partial \boldsymbol{U}} - \frac{\partial}{\partial \boldsymbol{U}}\int_0^T \int_\Omega \psi_p \nabla \cdot \boldsymbol{u}\, d\Omega\, dt + \frac{\partial}{\partial \boldsymbol{U}}\int_0^T \int_\Omega \boldsymbol{\psi_u} \cdot \left(\rho\left(\frac{\partial \boldsymbol{u}}{\partial t} + \boldsymbol{u}\cdot\nabla \boldsymbol{u}\right) - \nabla \cdot \boldsymbol{\sigma}\right) d\Omega\, dt. \tag{11}$$

The above relation, when set to zero, leads to a set of equations and boundary conditions that are used to evaluate the adjoint variables. This will be described in more detail in the following subsection. Variation of I with respect to $\boldsymbol{\Psi}$ gives back the flow Eqs. (1) and (2). The gradient, $\frac{\partial I}{\partial \boldsymbol{\beta}}$, is utilized to find the optimal shape parameters. It quantifies the sensitivity of the objective function to the design parameters. It is used by the optimizer to refine the search direction. The vanishing of the gradient reflects the attainment of optimal shape. The gradient is evaluated using the following expression:

$$\frac{\partial I}{\partial \boldsymbol{\beta}} = \frac{\partial I_c}{\partial \boldsymbol{\beta}} - \frac{\partial}{\partial \boldsymbol{\beta}}\int_0^T \int_\Omega \psi_p \nabla \cdot \boldsymbol{u}\, d\Omega\, dt + \frac{\partial}{\partial \boldsymbol{\beta}}\int_0^T \int_\Omega \boldsymbol{\psi_u} \cdot \left(\rho\left(\frac{\partial \boldsymbol{u}}{\partial t} + \boldsymbol{u}\cdot\nabla \boldsymbol{u}\right) - \nabla \cdot \boldsymbol{\sigma}\right) d\Omega\, dt. \tag{12}$$

3.2. The adjoint equations and related boundary and terminal conditions

The equations and boundary conditions for the adjoint variables are obtained by setting the variation of I with respect to the flow variables $\boldsymbol{U}$, given in Eq. (11), to zero. The equations governing the adjoint variables are:

$$\rho\left(-\frac{\partial \boldsymbol{\psi_u}}{\partial t} + (\nabla \boldsymbol{u})^T \boldsymbol{\psi_u} - (\boldsymbol{u}\cdot\nabla)\boldsymbol{\psi_u}\right) - \nabla \cdot \boldsymbol{\sigma_\psi} = 0 \quad \text{on } \Omega \times (0,T), \tag{13}$$

$$\nabla \cdot \boldsymbol{\psi_u} = 0 \quad \text{on } \Omega \times (0,T), \tag{14}$$

where, $\boldsymbol{\sigma_\psi}$ is similar to the stress tensor and is given by $\boldsymbol{\sigma_\psi} = -\psi_p \boldsymbol{I} + \mu[\nabla \boldsymbol{\psi_u} + (\nabla \boldsymbol{\psi_u})^T]$.

The boundary conditions on the adjoint variables are:

$$\boldsymbol{\psi_u} = 0 \quad \text{on } \Gamma_U, \tag{15}$$

$$\boldsymbol{s} = 0 \quad \text{on } \Gamma_D, \tag{16}$$

$$s_1 = 0, \quad \psi_{u2} = 0 \quad \text{on } \Gamma_S, \tag{17}$$

$$-\int_0^T \int_{\Gamma_B} \delta(\boldsymbol{\sigma}\cdot\boldsymbol{n})\cdot\boldsymbol{\psi_u}\, d\Gamma\, dt + \frac{\partial I_c}{\partial \boldsymbol{u}}\delta \boldsymbol{u} + \frac{\partial I_c}{\partial p}\delta p = 0 \quad \text{on } \Gamma_B, \tag{18}$$

where, $\boldsymbol{s} = \{\boldsymbol{u}\boldsymbol{\psi_u} - \boldsymbol{I}\psi_p + \nu[\nabla \boldsymbol{\psi_u} + (\nabla \boldsymbol{\psi_u})^T]\}.\boldsymbol{n}$. The terminal condition on the adjoint velocity is given by:

$$\boldsymbol{\psi_u}(\boldsymbol{u}, T) = 0 \quad \text{on } \Omega. \tag{19}$$

The adjoint equations (13) and (14) are a set of coupled linear partial differential equations. Unlike the flow equations (1) and (2), the equations for the adjoint variables are posed backward in time. In the present work, the adjoint variables are computed once the time integration of the flow equations has been carried out and results stored. It is possible to solve the flow and adjoint equations simultaneously [44,45]. However, this procedure can be computationally expensive and is not being used in the present work.

The conditions on the boundary, given by Eq. (18), depend on the definition of the objective function. This is illustrated with a few examples. The objective function to minimize the time-averaged drag coefficient is given by $I_c = \frac{1}{2}\overline{C_d}^2$. In this situation the boundary condition is given by

$$\boldsymbol{\Psi_u} = \left(-\frac{\overline{C_d}}{T}, 0\right) \quad \text{on } \Gamma_B \times (0,T).$$

Here, T is the time duration for which the aerodynamic coefficients are averaged and adjoints computed. Similarly, the objective function to maximize the ratio of the time-averaged lift coefficient to the time-averaged drag coefficient is given by $I_c = -\frac{1}{2}\left(\frac{\overline{C_l}}{\overline{C_d}}\right)^2$. In this case the boundary condition on Γ_B is given by

$$\boldsymbol{\Psi_u} = \left(-\frac{1}{T}\frac{\overline{C_l}^2}{\overline{C_d}^3}, \frac{1}{T}\frac{\overline{C_l}}{\overline{C_d}^2}\right) \quad \text{on } \Gamma_B \times (0,T).$$

4. Finite element formulation

4.1. Flow equations

The domain, Ω, is discretized into subdomains $\Omega^e, e = 1, 2, \ldots, n_{el}$, where n_{el} is the number of elements. A stabilized finite element method using piecewise linear interpolation functions for velocity and pressure is employed to discretize the governing equations (1) and (2). The trial and test function spaces are defined as:

$$\mathcal{S}_u^h = \left\{\boldsymbol{u}^h | \boldsymbol{u}^h \in (H^{1h})^{n_{sd}}, \boldsymbol{u}^h \doteq \boldsymbol{g}^h \text{ on } \Gamma_g\right\},$$
$$\mathcal{V}_u^h = \{\boldsymbol{w}^h | \boldsymbol{w}^h \in (H^{1h})^{n_{sd}}, \boldsymbol{w}^h \doteq \boldsymbol{0} \text{ on } \Gamma_g\},$$
$$\mathcal{S}_p^h = \mathcal{V}_p^h = \{q^h | q^h \in H^{1h}\}.$$

The function space $H^{1h}(\Omega)$ is given by:

$$H^{1h}(\Omega) = \{\phi^h | \phi^h \in C^0(\overline{\Omega}), \phi^h|_{\Omega^e} \in P^1\},$$

where, P^1 represent the first-order polynomials. The finite element formulation of the governing Eqs. (1) and (2) is as follows: find $\boldsymbol{u}^h \in \mathcal{S}_u^h$ and $p^h \in \mathcal{S}_p^h$ such that $\forall \boldsymbol{w}^h \in \mathcal{V}_u^h$ and $q^h \in \mathcal{V}_p^h$,

$$\int_\Omega \boldsymbol{w}^h \cdot \rho\left(\frac{\partial \boldsymbol{u}^h}{\partial t} + \boldsymbol{u}^h \cdot \nabla \boldsymbol{u}^h\right) d\Omega + \int_\Omega \epsilon(\boldsymbol{w}^h : \boldsymbol{\sigma}(p^h, \boldsymbol{u}^h))\, d\Omega + \int_\Omega q^h \nabla \cdot \boldsymbol{u}^h\, d\Omega + \sum_{e=1}^{n_{el}} \int_{\Omega^e} \frac{1}{\rho}(\tau_{SUPG}\rho \boldsymbol{u}^h \cdot \nabla \boldsymbol{w}^h + \tau_{PSPG}\nabla q^h)$$
$$\cdot \left[\rho\left(\frac{\partial \boldsymbol{u}^h}{\partial t} + \boldsymbol{u} \cdot \nabla \boldsymbol{u}\right) - \nabla \cdot \boldsymbol{\sigma}\right] d\Omega^e + \sum_{e=1}^{n_{el}} \int_{\Omega^e} \tau_{LSIC} \nabla \cdot \boldsymbol{w}^h \rho \nabla \cdot \boldsymbol{u}^h\, d\Omega^e = \int_{\Gamma^h} \boldsymbol{w}^h \cdot \boldsymbol{h}^h\, d\Gamma. \tag{20}$$

The first three terms and the right-hand side in the variational formulation given by Eq. (20) constitute the Galerkin formulation of the problem. The terms involving the element level integrals are the stabilization terms added to the basic Galerkin formulation to enhance its numerical stability. These terms stabilize the computations against node-to-node oscillations in advection dominated flows and allow the use of equal-in-order basis functions for velocity and pressure. The terms with coefficients τ_{SUPG} and τ_{PSPG} are based on the SUPG (Streamline-Upwind/Petrov–Galerkin) and PSPG (Pressure-stabilized/Petrov–Galerkin) stabilization. For the definition of these coefficients the interested reader is referred to the article by Tezduyar et al. [29]. The term with coefficient τ_{LSIC} is a stabilization term based on the least squares of the incompressibility constraint. Equal-in-order basis functions for velocity and pressure are used. A three point quadrature is employed for numerical integration. Marching in time is done via the generalized trapezoidal rule (Crank–Nicholson method).

4.2. Adjoint equations

A stabilized SUPG/PSPG finite element method is proposed to solve the adjoint Eqs. (13) and (14). The trial and test function spaces are defined as:

$$\mathcal{S}_{\psi_{\boldsymbol{u}}}^h = \{\boldsymbol{\psi}_u^h | \boldsymbol{\psi}_u^h \in (H^{1h})^{n_{sd}}, \boldsymbol{\psi}_u^h \doteq \boldsymbol{g}^h \text{ on } \Gamma_g\},$$
$$\mathcal{V}_{\psi_{\boldsymbol{u}}}^h = \{\boldsymbol{w}_{\psi_{\boldsymbol{u}}}^h | \boldsymbol{w}_{\psi_{\boldsymbol{u}}}^h \in (H^{1h})^{n_{sd}}, \boldsymbol{w}_{\psi_{\boldsymbol{u}}}^h \doteq 0 \text{ on } \Gamma_g\},$$
$$\mathcal{S}_{\psi_p}^h = \mathcal{V}_{\psi_p}^h = \{q_{\psi_p}^h | q_{\psi_p}^h \in H^{1h}\}.$$

The stabilized finite element formulation of Eqs. (13) and (14) is as follows: given $\boldsymbol{u}^h$ and $\boldsymbol{p}^h$ satisfying Eqs. (1) and (2), find $\boldsymbol{\psi}_u^h \in \mathcal{S}_{\psi_{\boldsymbol{u}}}^h$ and $\boldsymbol{\psi}_p^h \in \mathcal{S}_{\psi_p}^h$ such that $\forall \boldsymbol{w}_{\psi_{\boldsymbol{u}}}^h \in \mathcal{V}_{\psi_{\boldsymbol{u}}}^h$ and $q_{\psi_p}^h \in \mathcal{V}_{\psi_p}^h$,

$$\int_\Omega \boldsymbol{w}_{\psi_{\boldsymbol{u}}}^h \cdot \rho\left(-\frac{\partial \boldsymbol{\psi}_{\boldsymbol{u}}^h}{\partial t} + (\nabla \boldsymbol{u}^h)^T \boldsymbol{\psi}_{\boldsymbol{u}}^h - \boldsymbol{u} \cdot \nabla \boldsymbol{\psi}_{\boldsymbol{u}}\right) d\Omega + \int_\Omega \epsilon(\boldsymbol{w}_{\psi_{\boldsymbol{u}}}^h) : \boldsymbol{\sigma}_\psi(\psi_p^h, \boldsymbol{\psi}_{\boldsymbol{u}}^h)\, d\Omega + \int_\Omega q_{\psi_p}^h \nabla \cdot \boldsymbol{\psi}_{\boldsymbol{u}}^h d\Omega$$
$$+ \sum_{e=1}^{n_{el}} \int_{\Omega^e} \frac{1}{\rho}\left(\tau_{SUPG}(\rho\left(\nabla \boldsymbol{u}^{\boldsymbol{h}}\right)^T \boldsymbol{w}_{\psi_{\boldsymbol{u}}}^h - \rho \boldsymbol{u}^h \cdot \nabla \boldsymbol{w}_{\psi_{\boldsymbol{u}}}^h\right) + \tau_{PSPG} \nabla q_{\psi_p}^h\right)$$
$$\cdot \left[\rho\left(-\frac{\partial \boldsymbol{\psi}_{\boldsymbol{u}}^h}{\partial t} + (\nabla \boldsymbol{u}^{\boldsymbol{h}})^T \boldsymbol{\psi}_{\boldsymbol{u}}^h - \boldsymbol{u} \cdot \nabla \boldsymbol{\psi}_{\boldsymbol{u}}\right) - \nabla \cdot \boldsymbol{\sigma}_\psi(\psi_p^h, \boldsymbol{\psi}_{\boldsymbol{u}}^h)\right] d\Omega^e + \sum_{e=1}^{n_{el}} \int_{\Omega^e} \tau_{LSIC} \nabla \cdot \boldsymbol{w}_{\psi_{\boldsymbol{u}}}^h \rho \nabla \cdot \boldsymbol{\psi}_{\boldsymbol{u}}^h d\Omega^e = 0 \tag{21}$$

The stabilization coefficients τ_{SUPG}, τ_{PSPG} and τ_{LSIC} in the formulation proposed in Eq. (21) are computed based on the flow variables $(\boldsymbol{u}, p)$. For solving the adjoint equations, the flow solution is required at every time step. In the present work the flow solution is written to disk after every time step. After the time integration of flow equations has been carried out the adjoint solver reads the flow solution from the disk. The time spent in the input/output operations is found to be negligible compared to the overall solution time. This approach is expected to be very demanding on storage when extended to three-dimensions. To address the high demands on storage one can devise strategies based on ideas from information theory. For example, only the data corresponding to the critical sampling frequency from the Nyquist–Shannon sampling theorem [30] may be stored. The adjoint variables, for the intermediate time steps, can then be reconstructed from the stored flow via the Whittaker–Shannon

interpolation formula [31]. It is also possible to use proper orthogonal decomposition (POD) to reduce storage. The POD may be used to construct a basis for the unsteady flow. The storage of the basis is expected to be significantly cheaper than the storage of the entire unsteady flow data. Such an approach has been used in the context of optimal control of vortex shedding [32,33], control of flow separation over a forward facing step [34] and rocket nozzle flow control [35].

5. Implementation of the optimization procedure

A flow-chart listing the various steps in the optimization process in unsteady flows is shown in Fig. 2. The process has similarities with the one used by the authors for shape optimization in steady flows [15,36]. The details of the implementation are listed below:

1. *Initialize design parameters $\boldsymbol{\beta}$ and generate initial mesh.*The shape parameters, $\boldsymbol{\beta}$, that represent the surface to be optimized are identified. In the present work, NURBS (Non-Uniform Rational Bi-cubic Spline) is used to parameterize the surface. B-Splines, Bezier curves [37], Hicks and Henne functions [38] are a few other methods that can be used to represent the shape. Lepine et al. [39] state that one of the primary issues to be addressed in shape optimization is the determination of the least number of design variables that are capable of representing a large class of airfoil sections. They further note that any parametrization method that reduces the number of design parameters simplifies the design process as it significantly reduces the risk of noise. They suggest that a NURBS representation with 13 control points can be used to accurately represent a large family of airfoils. Fig. 3 shows the representation of a NACA0012 airfoil obtained by using 13 control points. The corresponding control polygon along with the control points are also shown. The control points at the leading edge and trailing edge are held fixed to preserve the chord length and angle of attack. The y-co-ordinates of the remaining control points are used as the design parameters. The difference between the resulting curve and the NACA0012 airfoil is less than 0.5% of the maximum thickness of the airfoil.A close-up view of the finite element mesh used for computations is shown in Fig. 4. The mesh consists of 44 804 nodes and 89 304 triangular elements with 200 nodes on the surface. A structured mesh is employed close to the airfoil surface and in the near wake to resolve the flow structures adequately. The remaining domain is filled with an unstructured mesh that is generated via Delaunay triangulation [40].
2. *Compute the unsteady flow, $\boldsymbol{u}$ and p and calculate the objective function I_c.*The finite element formulation given by Eq. (20) is utilized to compute the unsteady flow. The computed flow is used to compute I_c. The flow solution at all time steps is stored on the hard disk.
3. *Find $\psi_{\boldsymbol{u}}$ and ψ_p.*The finite element formulation given by Eq. (21) and the unsteady flow computed in previous step is utilized to compute the adjoint variables.
4. *Compute the gradient given by Eq. (12).*A finite difference approach, as described by Soto and Lohner [41] is used to calculate the gradient. The formula used is: $\frac{\partial I}{\partial \boldsymbol{\beta}} = \frac{I(\boldsymbol{\beta}+\Delta\boldsymbol{\beta})-I(\boldsymbol{\beta})}{\Delta\boldsymbol{\beta}}$. The value of $\Delta\boldsymbol{\beta}$ used in this work is 10^{-2}. Srinath and Mittal [36] carried out a study to investigate the effect of $\Delta\boldsymbol{\beta}$ in computing the gradient via a finite difference method. It was found that the round-off errors become significant for $\Delta\boldsymbol{\beta}$ smaller than 10^{-6}.

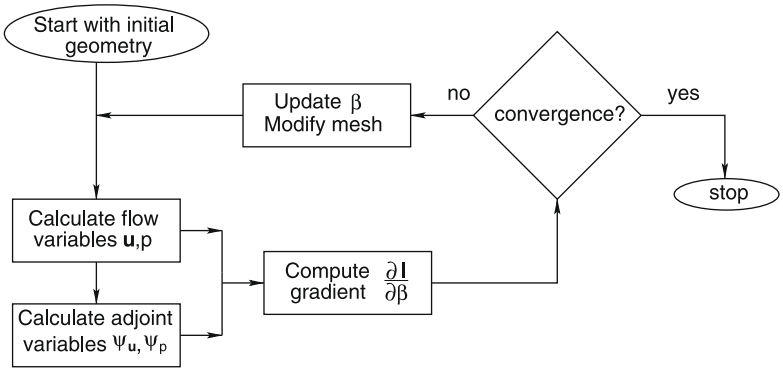

Fig. 2. A flow-chart detailing the steps of the optimization process.

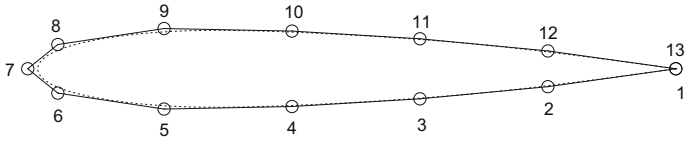

Fig. 3. Representation of NACA0012 airfoil with a NURBS curve. 13 control points are used and shown in the figure. Control points 1, 7 and 13 are held fixed and the y co-ordinates of remaining ten control points are used as design parameters. The broken line shows the resulting curve.

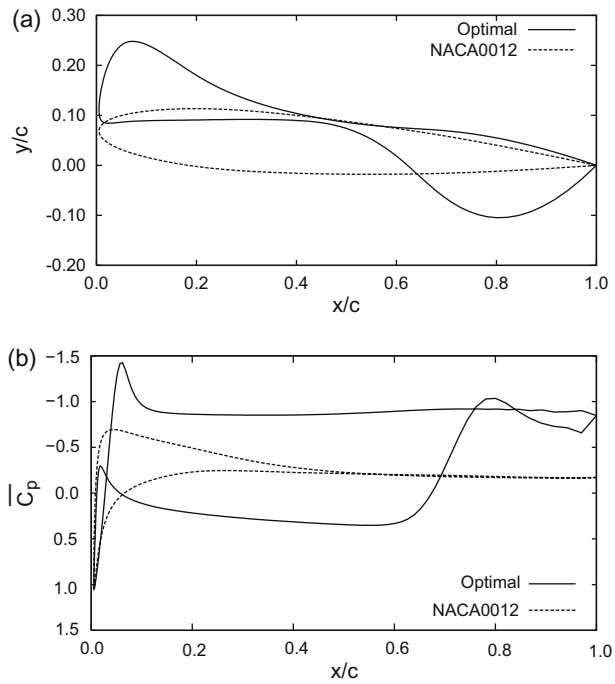

Fig. 6. Inverse design of airfoil for $\overline{C_l} = 0.75$ at $Re = 1000, \alpha = 4^\circ$: (a) initial and optimal shapes and (b) time-averaged C_p distribution.

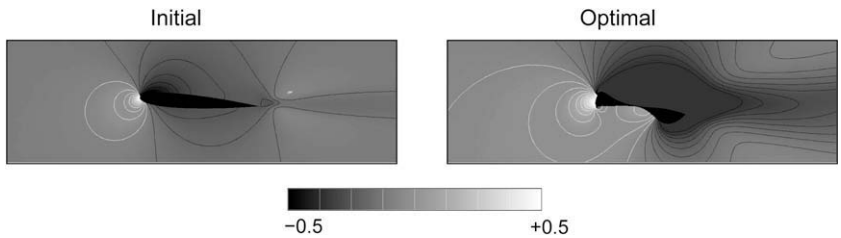

Fig. 7. Inverse design of airfoil for $\overline{C_l} = 0.75$ at $Re = 1000, \alpha = 4^\circ$: time-averaged pressure field for initial and optimal shapes.

with it, for reference, is the initial shape. The final shape has bulbous regions close to the leading and trailing edges with a narrow mid-chord portion. Also shown in Fig. 6(b) is the distribution of the time-averaged pressure coefficients for both the shapes. The value of the peak suction on the upper surface of the optimal airfoil is much larger than that on the NACA0012 airfoil. The pressure on the lower surface of the optimal airfoil is also larger. This leads to an increased time-averaged lift produced by the optimal airfoil. This is further seen from Fig. 7 which shows the time-averaged pressure field for the initial and optimal airfoils.

The iteration history of the objective function is shown in Fig. 8(a). Nine iterations are needed for the optimization process to converge to the desired accuracy. The iteration history of the time-averaged lift coefficient is shown in Fig. 8(b). Also shown are a few intermediate shapes obtained during the process. The resemblance between the final shape and that obtained at the end of first iteration of the optimization process is clearly seen. The subsequent iterations lead to finer changes in the shape, especially in the later half of the airfoil. The time histories of the lift and drag coefficients of the initial and optimal shapes are shown in Figs. 9(a) and (b). The vorticity field, for the initial and optimal shapes, at various time instants of the fully developed unsteady flow is shown in Fig. 10. The final shape is associated with larger unsteadiness than the NACA0012 airfoil. It is seen from the time histories of the lift coefficient shown in Fig. 9(a) that the frequency of vortex shedding for the optimal shape is significantly smaller than that for the NACA0012 airfoil. The optimal shape is associated with a much larger value of drag coefficient than the NACA0012 airfoil. The optimization process, for the unsteady flow leads to a significantly different shape than the one found for maximizing the lift coefficient for the steady flow at $Re = 500$ and $\alpha = 4^\circ$ reported in our earlier work [15]. Interestingly, the shape obtained for maximum C_l for the $\alpha = 4^\circ$ and $Re = 10$ flow is quite similar to the one reported here.

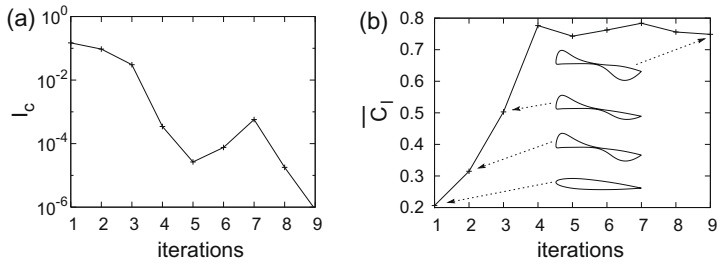

Fig. 8. Inverse design of airfoil for $\overline{C_l} = 0.75$ at $Re = 1000, \alpha = 4^d egr$: iteration history of the (a) objective function I_1 and (b) time-averaged lift coefficient with a few intermediate shapes.

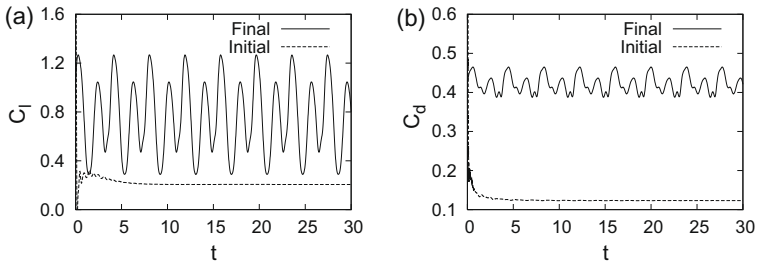

Fig. 9. Time histories of the aerodynamic coefficients for the initial and optimal shapes obtained for $\overline{C_l} = 0.75$ at $Re = 1000, \alpha = 4°$: (a) lift and (b) drag coefficient.

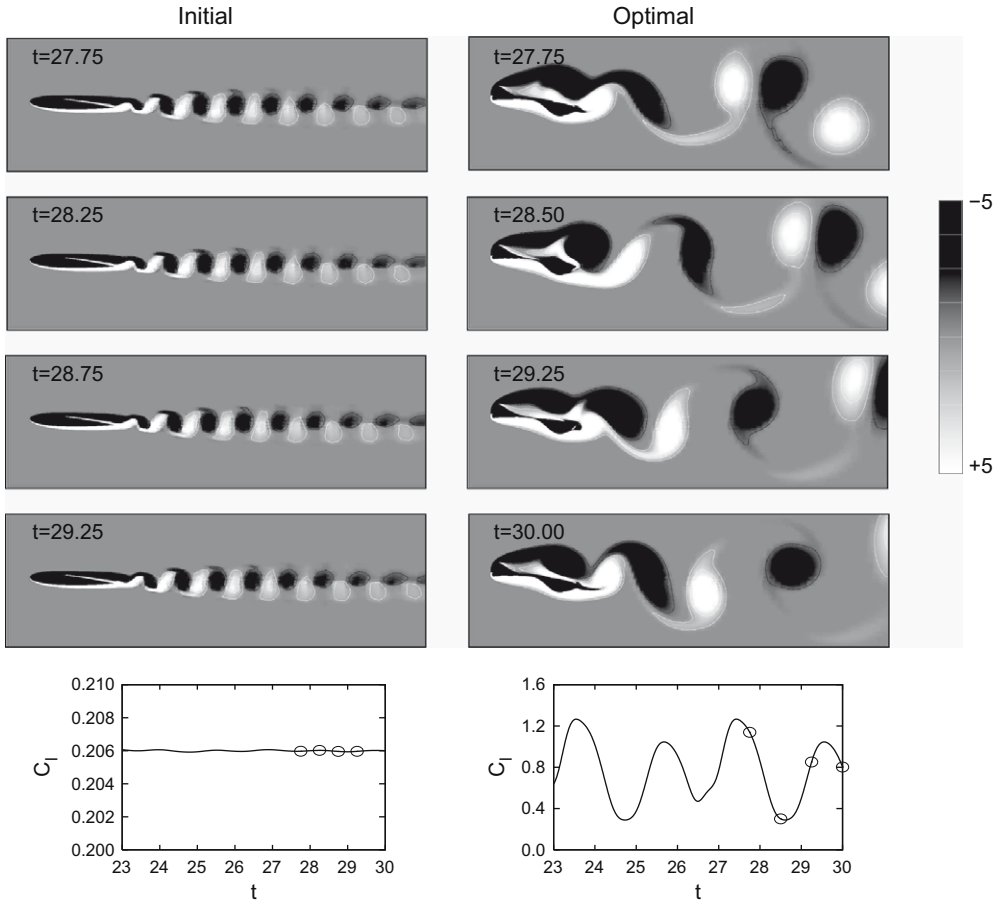

Fig. 10. Inverse design of airfoil for $\overline{C_l} = 0.75$ at $Re = 1000, \alpha = 4°$: vorticity field for the initial and optimal shapes at various time instants of the shedding cycle. The time instants at which the flow is shown are marked on the time history of the lift coefficient in the bottom row.

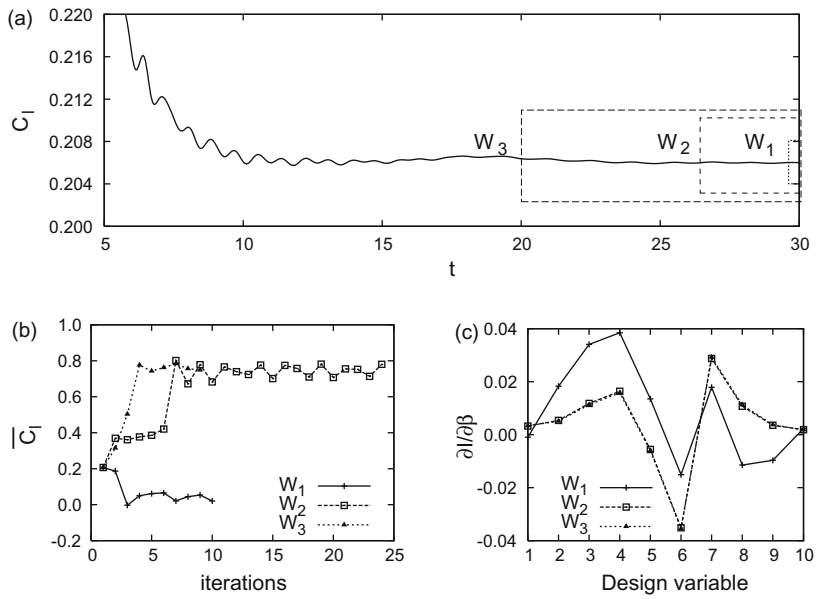

Fig. 11. Shape optimization of an airfoil for $Re = 1000, \alpha = 4^\circ$ and $\overline{C_l} = 0.75$: (a) time history of the lift coefficient for the NACA0012 airfoil along with the definition of the control windows, (b) iteration histories of $\overline{C_l}$ for the three control windows and (c) gradient of the objective function for all the design parameters for the first iteration of the design cycle.

6.2. Effect of T on optimization process

Figs. 9 and 10 show that while the C_l for the NACA0012 airfoil is almost steady, it is quite unsteady for the optimal shape. Since the time period of unsteadiness is not know a priori, one would like to carry out the time-averaging for each iteration in the design cycle for a sufficiently long time. A study is carried out to determine the effect of T on the optimization process. Three control windows, W_1, W_2, W_3 corresponding to 0.1, 3.0 and 10.0 time units, respectively, of the fully developed unsteady flow are chosen. These are shown in Fig. 11(a) for the time history of the NACA0012 airfoil. The convergence history of the time-averaged lift coefficient while using the three control windows is shown in Fig. 11(b). The optimizer diverges while using control window W_1. It proceeds in the correct direction while using control window W_2, but does not converge to the required accuracy even after 24 design cycles. Convergence criteria is satisfied in merely nine design cycles with the control window W_3.

To investigate the cause of this behaviour we study the gradients obtained for the three control windows at the end of the first design cycle. Fig. 11(c) shows the value of the gradient, $\frac{\partial I}{\partial \beta}$, for each of the ten design variables. Eq. (12) shows that the contribution to $\frac{\partial I}{\partial \beta}$ comes from $\frac{\partial I_c}{\partial \beta}$ as well as the constraint equations. For the first design iteration the flow and the adjoints are for the initial shape: the NACA0012) airfoil. Since the C_l is almost steady, the contribution of $\frac{\partial I_c}{\partial \beta}$ to the gradient is virtually the same for all the three control windows. The difference in $\frac{\partial I}{\partial \beta}$, for the three control windows, is therefore from the constraint equations. Gradients obtained using control window W_1 not only have different magnitude, but for many of the design variables (5, 8 and 9 as seen in Fig. 11(c)), the sign is also different from those obtained using control windows W_2 and W_3. The gradients from W_2 and W_3 are seen to be very close to each other. Control windows W_2 and W_3 correspond to 1 and 3 vortex shedding cycles of the optimal shape, approximately. These computations confirm that the gradients are expected to be well represented if either one uses a window that spans an exact integral multiple of number of time periods of a periodic solution or employs a window that spans a long time duration. As is the case in W_1, a window that spans a small fraction of the time period of an unsteady solution, computations may lead to inaccurate gradients, and therefore, an inaccurate trajectory of the design cycle. All the computations in this study have been carried out with control window W_3.

6.3. Effect of geometric constraint on optimization process

A geometric constraint is imposed on the inverse design problem. The objective is to determine an airfoil with a time-averaged lift coefficient of 0.75 and a certain volume The objective function is given by $I_c = \frac{1}{2}(\overline{C_l} - 0.75)^2 + \gamma \frac{1}{2}(V - V_0)^2$. Here V_0 is set to 0.05. The weight, γ, is required to ensure that both the terms in the objective function contribute, approximately, equally. If γ is too small, the volume constraint may get overwhelmed by the condition on $\overline{C_l}$. On the other hand, it is too large, then the error in the satisfaction of the objective function may be borne largely by the satisfaction of the condition on $\overline{C_l}$. This has been addressed in the context of steady flows in an earlier article [15]. Computations are carried out for various values of γ. The error in satisfaction of lift and volume enclosed is less than 4%. The value of γ for these computations is

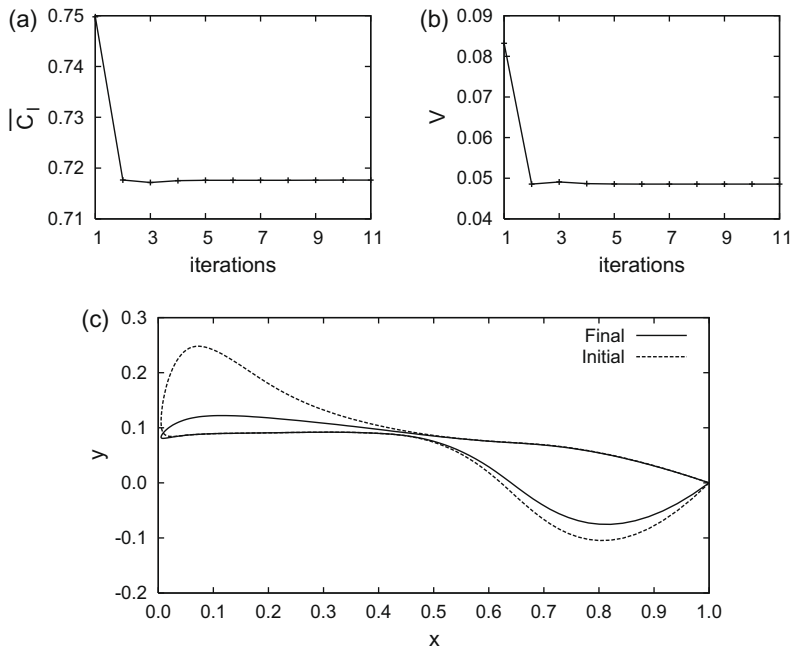

Fig. 12. Inverse design of airfoil for $\overline{C_l} = 0.75, V_0 = 0.05$ and $\alpha = 4^\circ$ at $Re = 1000$: (a) iteration history of time averaged lift coefficient, (b) volume enclosed and (c) initial and final shapes.

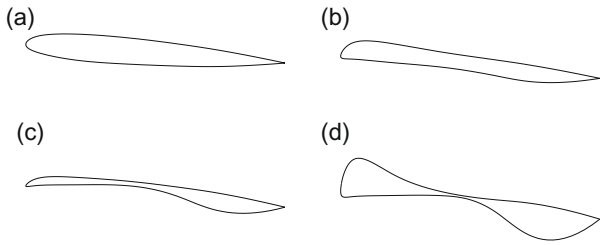

Fig. 13. $Re = 1000, \alpha = 4^\circ$, optimal shapes obtained for various values of $\overline{C_l}$: (a) 0.25, (b) 0.35, (c) 0.5 and (d) 0.65.

10. The optimal airfoil for $I_c = \frac{1}{2}(\overline{C_l} - 0.75)^2$ is used as the initial guess. Fig. 12 shows the iteration history of the time-averaged lift coefficient and volume of the airfoil. The final and initial shapes are shown in Fig. 12(c). Unlike the initial shape, which has a thick leading edge, the final shape has a thinner leading edge.

6.4. Inverse design for various $\overline{C_l}$

The airfoil shape obtained from inverse design for $\overline{C_l} = 0.75$, and shown in Fig. 6 appears non-intuitive. To investigate this further, the design is repeated for lower values of $\overline{C_l}$: 0.25, 0.35, 0.5 and 0.65. The shapes obtained for these cases are shown in Fig. 13. The $\overline{C_l}$ for the NACA 0012 airfoil at $\alpha = 4^\circ$ is 0.2. As expected, the geometry obtained for $\overline{C_l} = 0.25$ is very similar to the NACA 0012 airfoil. However, significant departure from the NACA 0012 airfoil geometry is seen for higher values of $\overline{C_l}$. Starting from the base NACA 0012 geometry the increase in lift is first obtained via modification of the fore section of the airfoil. This is followed by modification in the aft section on the lower surface. The shapes for $\overline{C_l} = 0.65$ and 0.75 are very similar. This shows that when an ambitious objective is posed, the optimizer is able meet it but with shapes that seem non-intuitive.

Fig. 14 shows the time histories of C_l for the various optimal shapes. The flow is virtually steady for shapes with $\overline{C_l} = 0.25$, 0.35 and 0.5. However, significant unsteadiness is observed for the shape with $\overline{C_l} = 0.65$. The frequency of vortex shedding for the flows with $\overline{C_l} = 0.65$ and 0.75 are very similar. Fig. 15 shows the chord wise distribution of the time-averaged pressure coefficient for the various cases studied. In general, the suction on the upper surface of the airfoil increases with increase in $\overline{C_l}$. However, the peak suction appears to depend on how bulbous the leading edge is. Fig. 16 shows the time-averaged pressure field for the various optimal airfoils. Increase in zone of suction, close to the upper surface of the airfoil, with

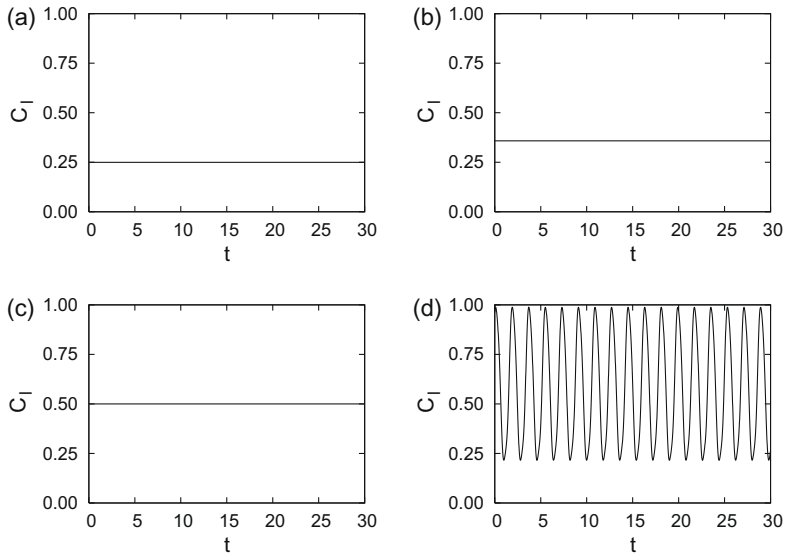

Fig. 14. $Re = 1000, \alpha = 4^{\circ}$, time histories of C_l for the optimal shapes obtained for various values of $\overline{C_l}$: (a) 0.25, (b) 0.35, (c) 0.5 and (d) 0.65.

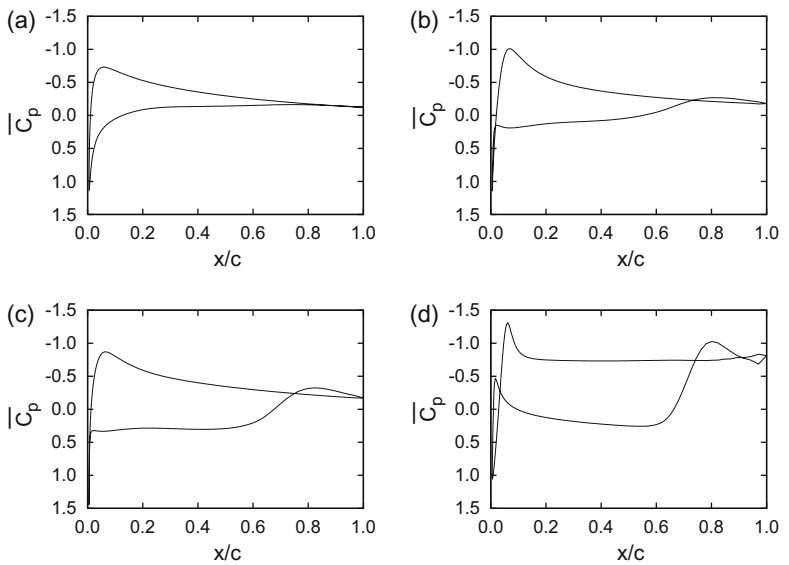

Fig. 15. $Re = 1000, \alpha = 4^{\circ}$, time-averaged C_p distribution for the optimal shapes obtained for various values of $\overline{C_l}$: (a) 0.25, (b) 0.35, (c) 0.5 and (d) 0.65.

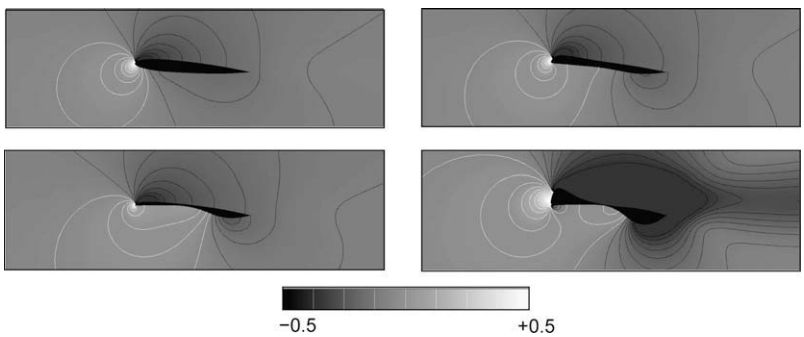

Fig. 16. $Re = 1000, \alpha = 4^{\circ}$, time-averaged pressure field for the optimal shapes obtained for various values of $\overline{C_l}$: (a) 0.25, (b) 0.35, (c) 0.5 and (d) 0.65.

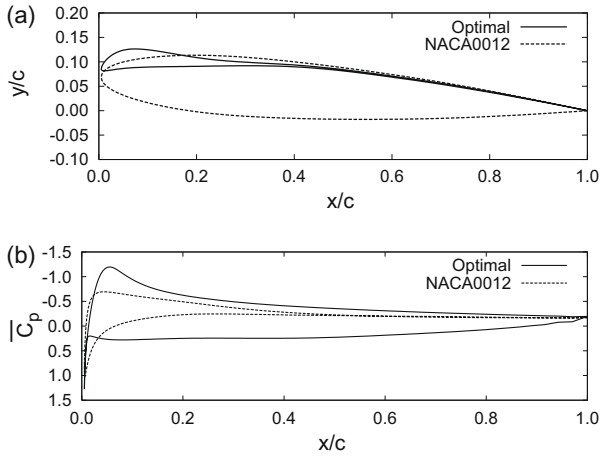

Fig. 17. Minimization of the time-averaged drag to lift ratio at $Re = 1000, \alpha = 4^\circ$: (a) initial and final shapes and (b) time-averaged C_p distribution.

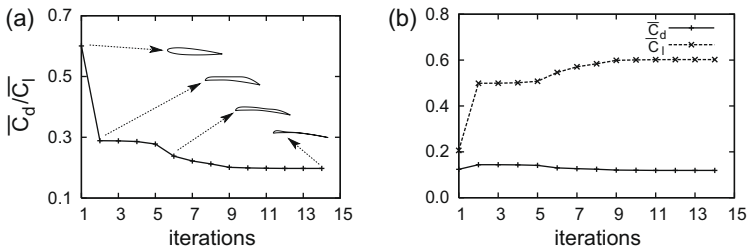

Fig. 18. Minimization of the time-averaged drag to lift ratio at $Re = 1000, \alpha = 4^\circ$: (a) iteration history of $\overline{C_d}/\overline{C_l}$ and (b) iteration history of $\overline{C_d}$ and $\overline{C_l}$.

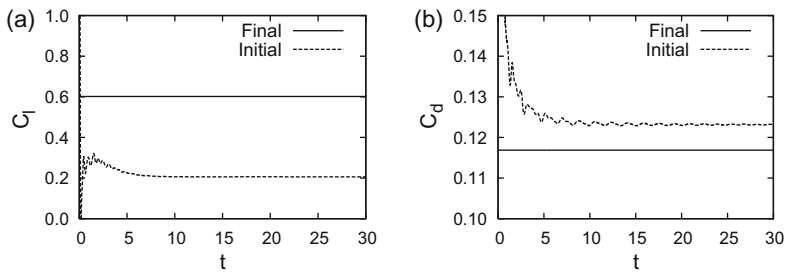

Fig. 19. Minimization of the time-averaged drag to lift ratio at $Re = 1000, \alpha = 4^\circ$: (a) time history of lift coefficient for initial and final shapes and (b) time history of drag coefficient for initial and final shapes.

increase in $\overline{C_l}$ is observed. Also seen is an overall increase in the pressure on the lower surface of the airfoil. This is also observed in the $\overline{C_p}$ distribution shown in Fig. 15. Shapes for $\overline{C_l} = 0.35$ and 0.65 have a relatively thicker leading edge compared to the ones for $\overline{C_l} = 0.25$ and 0.5. The airfoil with $\overline{C_l} = 0.5$ exhibits a bulbous region on the lower surface close to the trailing edge. This seems to be the cause of larger pressure on the lower surface and the increased time-averaged lift. The airfoils for $\overline{C_l} = 0.65$ as well $\overline{C_l} = 0.75$ have a bulbous region close to the leading as well as trailing edge.

6.5. Direct objective function: minimization of $(\overline{C_d}/\overline{C_l})$

This example involves determining the airfoil that minimizes the time-averaged drag to lift ratio at $Re = 1000$. The objective function is given by $I_c = \frac{1}{2}\left(\frac{\overline{C_d}}{\overline{C_l}}\right)^2$. The initial and final shapes are shown in Fig. 17(a). The final shape is akin to a curved plate with a bulbous leading edge. The C_p distribution, shown in Fig. 17(b), for the optimal shape shows a slightly large suction zone on the upper surface. The lower surface exhibits higher pressure for the optimal shape. The iteration history of the

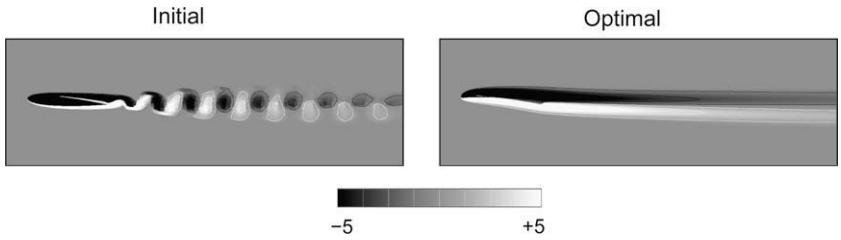

Fig. 20. Design of airfoil for $\overline{C_d}/\overline{C_l}$ at $Re = 1000, \alpha = 4^\circ$: Vorticity contours for the initial and optimal shapes at $t = 27.75$. The flow over the optimal shape achieves a steady state.

time-averaged drag to lift ratio is shown in Fig. 18(a). The NACA0012 airfoil at $Re = 1000$ and $\alpha = 4^\circ$ has a drag to lift ratio of 0.6. At the end of the optimization process, the ratio of drag to lift is reduced to 0.2. The optimizer required 14 design cycles to achieve this value. The iteration history of the time-averaged drag and lift coefficients is shown in Fig. 18(b). The optimal shape has 4% lesser drag than the NACA0012 airfoil, while it generates 3 times more lift. Figs. 19(a) and 19(b) show the time histories of the lift and drag coefficient, respectively. The vorticity field for the initial and final shapes is shown in Fig. 20. Unlike for the NACA0012 airfoil, the flow for the optimal shape achieves a steady state.

7. Conclusions

A new method, based on the time accurate continuous adjoint approach, for shape optimization for unsteady viscous flows has been presented in this paper. The time accurate continuous adjoint equations have been derived. The boundary conditions for the adjoint equations are generated for various objective functions. A stabilized finite element method based on the SUPG/PSPG stabilization has been used to solve, both, flow and the adjoint equations. The airfoil is represented by a NURBS curve. The y-co-ordinates of the control points have been used as design variables. To validate the algorithm, two test cases have been carried out. Both the cases involve enhancing the time-averaged aerodynamic coefficients of an airfoil at $Re = 1000$ and $\alpha = 4^\circ$. For both the cases, NACA0012 airfoil has been used as the initial guess.

The first test case involves an inverse objective function on the time-averaged lift coefficient. The objective is to obtain an airfoil that has a time-averaged lift coefficient of 0.75. The optimizer is able to obtain the required solution within nine design iterations. A study is carried out to determine the effect of extent of the window of time integration of flow and adjoint equations on the design process. It is found that too small a window leads to inaccurate gradients which in turn result in an inaccurate search direction and degradation of the convergence of optimization cycle.

The shapes of airfoils for relatively low values of time-averaged lift coefficient are very similar to conventional airfoils. Non-intuitive shapes are obtained for large values of $\overline{C_l}$. The second test case involves a direct objective function on the time-averaged drag to lift ratio. An airfoil that has 67% less drag to lift than the initial NACA0012 airfoil is obtained. These examples demonstrate the potential of the proposed method to optimize aerodynamic shapes in unsteady flow.

References

[1] S. Obyashi, Aerodynamic inverse optimization with genetic algorithms, Journal of Engineering and Applied Science (1996) 421–425.
[2] C.O.E. Burg, J.C. Newman III, Computationally efficient, numerically exact design derivatives via the complex Taylor series expansion method, Computers and Fluids 32 (2003) 373–383.
[3] L.L. Sherman, V.C. Taylor III, L.L. Green, P.A. Newman, G.J.W. Hou, M. Korivi, First and second order aerodynamic sensitivity derivatives via automatic differentiation with incremental iterative methods, Journal of Computational Physics 129 (1994) 307–331.
[4] G.J.W. Hou, J.S. Sheen, C.H. Chuang, Shape sensitivity analysis and design optimization of linear thermoelastic solids, AIAA Journal 30 (1992) 528–537.
[5] B. Mohammadi, O. Pironneau, Shape optimization in fluid mechanics, Annual Review of Fluid Mechanics 36 (2004) 255–279.
[6] M.B. Giles, N.A. Pierce, An introduction to the adjoint approach to design, Flow Turbulence and Combustion 65 (2000) 393–415.
[7] A. Jameson, Aerodynamic design via control theory, Journal of Scientific Computing 59 (1988) 117–128.
[8] W.K. Anderson, V. Venkatakrishnan, Aerodynamic design optimization on unstructured grids with a continuous adjoint formulation, Computers and Fluids 28 (4–5) (1999) 443–480.
[9] B. Mohammadi, Optimization of aerodynamic and acoustic performances of supersonic civil transports, International Journal for Numerical Methods in Fluids 14 (2004) 891–907.
[10] J. Reuthers, A. Jameson, J. Farmer, L. Martinelli, D. Saunders, Aerodynamic shape optimization of complex aircraft configurations via adjoint formulations, AIAA Paper 96-0094, 1996.
[11] A. Jameson, Computational aerodynamics for aircraft design, Science 245 (1989) 361–371.
[12] S. Nadarajah, O. Soucy, C. Balloch, Sonic boom reduction via remote inverse adjoint approach, AIAA Paper 07-0056, 2007.
[13] O. Soto, R. Lohner, C. Yang, An adjoint-based design methodology for CFD problems, International Journal of Numerical Methods for Heat and Fluid Flow 14 (2004) 734–759.
[14] F. Abraham, M. Behr, M. Heinkenschloss, Shape optimization in steady blood flow: a numerical study of non-Newtonian effects, Computer Methods in Biomechanics and Biomedical Engineering 8 (2005) 127–137.
[15] D.N. Srinath, S. Mittal, Optimal airfoil shapes for low Reynolds number flows, International Journal for Numerical Methods in Fluids 61 (2009) 353–381.
[16] J.-W. He, R. Glowinski, R. Metcalfe, A. Nordlander, J. Periaux, Active control and drag optimization for flow past a circular cylinder, Journal of Computational Physics 163 (2000) 83–117.

[17] C. Homescu, I.M. Navon, Z. Li, Suppression of vortex shedding for flow control around a circular cylinder using optimal control, International Journal for Numerical Methods in Fluids 38 (2002) 43–69.
[18] H. Okumura, M. Kawahara, Shape optimization of a body located in incompressible Navier–Stokes flow based on optimal control theory, Computer Modelling in Engineering and Sciences 1 (2000) 71–77.
[19] S.K. Nadarajah, A. Jameson, Optimum shape design for unsteady flows with time accurate continuous and discrete adjoint methods, AIAA Journal 45 (2007) 1478–1491.
[20] K. Mani, D.J. Mavriplis, Unsteady discrete adjoint formulation for two-dimensional flow problems with deforming meshes, AIAA Journal 46 (2008) 1351–1364.
[21] M.P. Rumpfkeil, D.W. Zingg, A general framework for the optimal control of unsteady flows with applications, AIAA 07-1128, 2007.
[22] M.P. Rumpfkeil, D.W.Zingg, The optimal control of unsteady flows with a discrete adjoint method, Optimization and Engineering (2008), doi:10.1007/s11081-008-9035-5.
[23] S.S. Collis, K. Ghayour, M. Heinkenschloss, M. Ulbrich, S. Ulbrich, Optimal control of unsteady viscous compressible flow, International Journal for Numerical Methods in Fluids 40 (2002) 1401–1428.
[24] K.C. Hall, W.S. Clark, Linearized Euler predictions of unsteady aerodynamic loads in cascades, AIAA Journal 31 (1993) 540–550.
[25] M. McMullen, A. Jameson, J.J. Alonso, Application of non-linear frequency domain solver to the Euler and Navier–Stokes equations, AIAA 02-0120, 2002.
[26] M.C. Duta, M.B. Giles, M.S. Campobasso, The harmonic adjoint approach to unsteady turbomachinery design, International Journal for Numerical Methods in Fluids 40 (2002) 323–332.
[27] S.K. Nadarajah, M.S. McMullen, A.J. Jameson, Optimum shape design for unsteady flows using time accurate and non-linear frequency domain methods, AIAA Paper 2003-3875, 2002.
[28] S.K. Nadarajah, C. Tatossian, Multi-objective aerodynamic shape optimization for unsteady viscous flows. Optimization and Engineering (2008), doi:10.1007/s11081-008-9036-4.
[29] T.E. Tezduyar, S. Mittal, S.E. Ray, R. Shih, Incompressible flow computations with stabilized bilinear and linear equal order interpolation velocity pressure elements, Computer Methods in Applied Mechanics and Engineering 95 (1992) 221–242.
[30] P.P. Vaidyanathan, Generalizations of the sampling theorem: seven decades after Nyquist, IEEE Transactions on Circuits and Systems I: Fundamental Theory and Applications 48 (9) (2001) 1094–1109.
[31] A.J. Jerri, Shannon sampling theorem – its various extensions and applications: a tutorial review, Proceedings of the IEEE 65 (11) (1977) 1565–1596.
[32] W.R. Graham, J. Peraire, K.Y. Tang, Optimal control of vortex shedding using low-order models. Part I – Open-loop model development, International Journal for Numerical Methods in Engineering 44 (7) (1999) 945–972.
[33] M. Bergmann, L. Cordier, Optimal control of the cylinder wake in the laminar regime by trust-region methods and POD reduced-order models, Journal of Computational Physics 227 (16) (2008) 7813–7840.
[34] S.S. Ravindran, Control of flow separation over a forward-facing step by model reduction, Computer Methods in Applied Mechanics and Engineering 191 (41–42) (2002) 4599–4617.
[35] D.J. Lucia, M. Pachter, P.S. Beran, Rocket nozzle flow control using a reduced-order computational fluid dynamics model, Journal of Guidance Control and Dynamics 25 (3) (2002) 449–454.
[36] D.N. Srinath, S. Mittal, A stabilized finite element method for shape optimization in low Reynolds number flows, International Journal for Numerical Methods in Fluids 54 (2007) 1451–1471.
[37] Gerald Farin, Curves and Surfaces for Computer Aided Geometric Design. A Practical Guide, Academic Press, San Diego, USA, 1990.
[38] R.M. Hicks, P.A. Henne, Wing design by numerical optimization, Journal of Aircraft 15 (1978) 407–412.
[39] J. Lepine, F. Guibault, J. Trepanier, F. Pepin, Optimized nonuniform rational B-spline geometrical representation for aerodynamic design of wings, AIAA Journal 39 (11) (2001) 2033–2041.
[40] H. Borouchaki, P.L. George, Aspects Of 2-D Delaunay mesh generation, International Journal for Numerical Methods in Engineering 40 (1997) 1957–1975.
[41] O. Soto, R. Lohner, CFD shape optimization using an incomplete-gradient adjoint formulation, International Journal of Numerical Methods in Engineering 51 (2001) 735–753.
[42] R.H. Byrd, P. Lu, J. Nocedal, C. Zhu, A limited memory algorithm for bound constrained optimization, SIAM Journal of Scientific Computing 16 (1995) 1190–1208.
[43] T.E. Tezduyar, M. Behr, S. Mittal, A.A. Johnson, Computation of unsteady incompressible flows with the finite element methods – space–time formulations, iterative strategies and massively parallel implementations, in: P. Smolinski, W.K. Liu, G. Hulbert, K. Tamma (Eds.), New Methods in Transient Analysis, AMD-Vol. 143, ASME, New York, 1992, pp. 7–24.
[44] G. Kuruvilla, S. Taasan, M.D. Salas, Airfoil design and optimization by the one-shot method, AIAA Paper 95-0478, 1995.
[45] MD. Gunzburger, Sensitivities adjoints and flow optimization, International Journal for Numerical Methods in Fluids 31 (1999) 53–78.
[46] O.C. Zienkiewicz, J.Z. Zhu, Simple error estimator and adaptive procedure for practical engineering analysis, International Journal for Numerical Methods in Fluids 24 (2) (1987) 337–357.